



Characteristics of Slow Slip Event in March 2020 Revealed From Borehole and DONET Observatories

Keisuke Ariyoshi^{1*}, Takeshi Iinuma¹, Masaru Nakano¹, Toshinori Kimura¹, Eiichiro Araki¹, Yuya Machida¹, Kentaro Sueki¹, Shuichiro Yada¹, Takehiro Nishiyama¹, Kensuke Suzuki², Takane Hori¹, Narumi Takahashi^{1,3} and Shuichi Kodaira¹

¹Japan Agency for Marine-Earth Science and Technology, Yokohama, Japan, ²Sendai Regional Headquarters, Japan Meteorological Agency, Sendai, Japan, ³National Research Institute for Earth Science and Disaster Resilience, Tsukuba, Japan

OPEN ACCESS

Edited by:

Keiichi Tadokoro,
Nagoya University, Japan

Reviewed by:

Michel Campillo,
Université Grenoble Alpes, France
Norio Matsumoto,
National Institute of Advanced
Industrial Science and Technology
(AIST), Japan

*Correspondence:

Keisuke Ariyoshi
ariyoshi@jamstec.go.jp

Specialty section:

This article was submitted to
Solid Earth Geophysics,
a section of the journal
Frontiers in Earth Science

Received: 31 August 2020

Accepted: 07 December 2020

Published: 22 January 2021

Citation:

Ariyoshi K, Iinuma T, Nakano M,
Kimura T, Araki E, Machida Y, Sueki K,
Yada S, Nishiyama T, Suzuki K, Hori T,
Takahashi N and Kodaira S (2021)
Characteristics of Slow Slip Event in
March 2020 Revealed From Borehole
and DONET Observatories.
Front. Earth Sci. 8:600793.
doi: 10.3389/feart.2020.600793

We have detected an event of pore pressure change (hereafter, we refer it to “pore pressure event”) from borehole stations in real time in March 2020, owing to the network developed by connecting three borehole stations to the Dense Oceanfloor Network System for Earthquakes and Tsunamis (DONET) observatories near the Nankai Trough. During the pore pressure event, shallow very low-frequency events (sVLFs) were also detected from the broadband seismometers of DONET, which suggests that the sVLF migrated toward updip region along the subduction plate boundary. Since one of the pore pressure sensors have been suffered from unrecognized noise after the replacement of sensors due to the connecting operation, we assume four cases for crustal deformation component of the pore pressure change. Comparing the four possible cases for crustal deformation component of the volumetric strain change at C0010 with the observed sVLF migration and the characteristic of previous SSEs, we conclude that the pore pressure event can be explained from SSE migration toward the updip region which triggered sVLF in the passage. This feature is similar to the previous SSE in 2015 and could be distinguished from the unrecognized noise on the basis of *t*-test. Our new finding is that the SSE in 2020 did not reach very shallow part of the plate interface because the pore pressure changes at a borehole station installed in 2018 close to the trough axis was not significant. In the present study, we estimated the amount, onset and termination time of the pore pressure change for the SSE in 2020 by fitting regression lines for the time history. Since the change amount and duration time were smaller and shorter than the SSE in 2015, respectively, we also conclude that the SSE in 2020 had smaller magnitude than the SSE in 2015. These results would give us a clue to monitor crustal deformation along the Nankai Trough directly from other seafloor observations.

Keywords: shallow very low-frequency event (sVLF), slow earthquake, Nankai trough, pore pressure, seafloor leveling change, crustal deformation

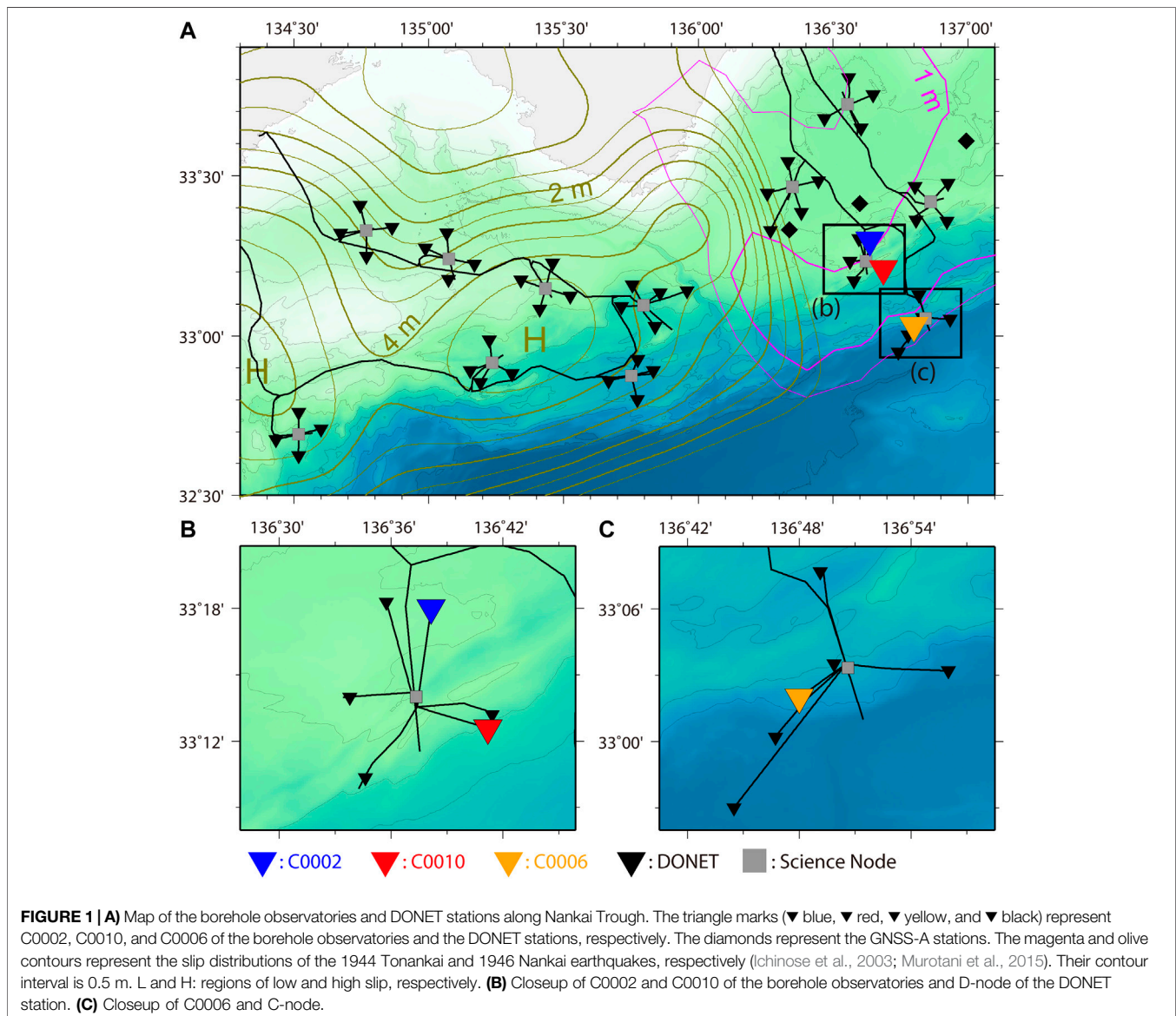
INTRODUCTION

In the wake of the 2004 Sumatra-Andaman earthquake (e.g., Wiseman and Bürgmann, 2011), the Japanese government has established seafloor networks of cable-linked observatories around Nankai Trough (**Figure 1**): DONET (Dense Oceanfloor Network system for Earthquakes and Tsunamis along the Nankai Trough) which has sensors of broadband seismogram, strong ground motion, and hydraulic pressure (e.g., Kaneda et al., 2015; Kawaguchi et al., 2015). DONET has been expected to monitor the propagation process of tsunami (e.g., Maeda et al., 2015) and seismic waves (Nakamura et al., 2015) as well as seismic activity (Nakano et al., 2016; 2018) in real time.

Owing to inland dense networks of seismic and geodetic observations have revealed that slow earthquakes occur along the subduction plate boundaries in the shallower and deeper extensions

of megathrust earthquake source regions worldwide (e.g., Schwartz and Rokosky, 2007; Obara and Kato, 2016). Slow earthquake is assumed to be classified into several types according to the spatiotemporal scale (Ide et al., 2007). For example, low-frequency tremor and very low-frequency events (VLFs) have dominant periods of approximately several hertz (Obara, 2002) and 10–100s (Ito et al., 2007), respectively, whereas slow slip events (SSEs) have a duration time of days to years (Dragert et al., 2001).

As a Japanese governmental organization, Earthquake Research Committee of the Headquarters for Earthquake Research Promotion (2013) has pointed out the possibility of megathrust earthquakes occurring along Nankai in the near future. Slow earthquake is more sensitive to stress change than a regular earthquake (Obara and Kato, 2016); hence, it is important to monitor slow earthquake activities close to a megathrust earthquake. Some numerical simulations have demonstrated that the recurrence interval and the moment

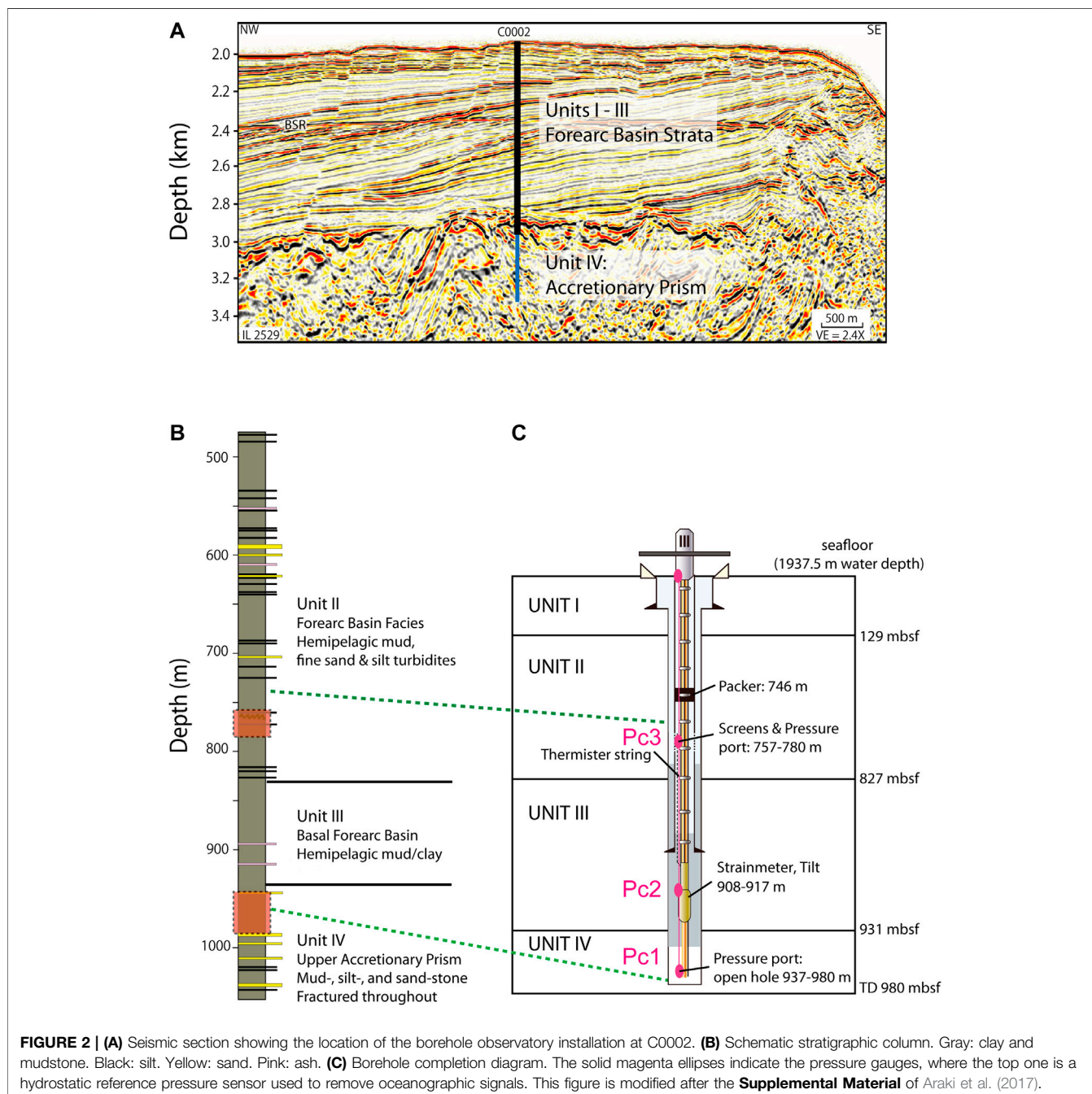


release rate of VLFs/SSEs become shorter and higher, respectively, in the pre-seismic stage of a megathrust earthquake (Matsuzawa et al., 2010; Ariyoshi et al., 2012).

For the shallower slow earthquakes occurred in the shallower extension, these changes are expected to be larger than those in the deeper one from numerical simulation study (Ariyoshi et al., 2014a; Ariyoshi et al., 2014b). Shallower VLFs near the trench (sVLFs) has been detected around the Nankai Trough not only by seafloor cabled networks (Nakano et al., 2016; Nakano et al., 2018; Nishikawa et al., 2019) but also by inland seismic networks (Takemura et al., 2019). By contrast, the shallower SSE near the

trench has so far been detected only from the pore pressure change of the borehole observatories (Wallace et al., 2016; Araki et al., 2017) and the seafloor global navigation satellite system-acoustic (GNSS-A) (Ishikawa et al., 2020) because the SSE can be detected by static crustal deformation with distance r^{-3} decay, which is too small for inland GNSS networks. However, the data of the borehole observatories at that time were offline. GNSS-A is also offline, and its time resolution of the SSE signal detection is 0.2 years (Yokota and Ishikawa, 2020).

Recently, the borehole observatories in holes C0002 (Figure 2), C0010, and C0006 were successfully connected to



DONET: C0002 in January 2013 (Kitada et al., 2013), C0010 in April 2016 (Saffer et al., 2017), and C0006 in March 2018. This operation has enabled us to monitor crustal deformation along the Nankai Trough in real time. Afterward, in the latter part of March 2020 (**Figure 3**), significant change of pore pressure (we refer to “pore pressure event”) and five sVLFs were detected by the borehole site C0002 and broadband seismometers of DONET, respectively. On the other hand, there is no signal at C0006. For C0010, there appears pore pressure change during that time, but it seems not to be stable before and after that period. This instability began after the replacement operation of the sensors, which means the possibility that the record of the pore pressure at C0010 contains both crustal deformation and other unrecognized fluctuations. Therefore, it is very important to examine whether those changes could be explained by a reasonable fault model of SSE or not. In the present study, we first reviewed the pore pressure change and sVLF activity. Next, we investigate the time history of pore pressure change at C0002 by fitting regression lines. Using these results, we try to find reasonable fault models for the pore pressure event by considering possible cases of pore pressure change at C0010, the observed sVLF, and the characteristics of previous SSEs when C0010 was stable. To evaluate the reliability of pore pressure record at C0010, we conduct *t*-test between the pore pressure event and the unrecognized fluctuation for yearlong data before the pore pressure event. Finally, we discussed the detectability of the seafloor crustal deformation caused by the possible fault models, toward monitoring the plate coupling around the Nankai Trough.

PORE PRESSURE CHANGE AT BOREHOLES

Three borehole observatories (i.e., C0002, C0010, and C0006) in the sedimentary wedge can be found above the subduction plate boundary in the Nankai Trough. An overview of the observatory station at C0002, which is the main target of the present study, is shown in **Figure 2**. We have continuously monitored the crustal deformations, using the pore pressure changes observed by the sensors installed in finely grained sediments with low

permeability. For each observatory, two or three sensors were installed at hydraulically isolated depth intervals (C0002: 1966 m depth below sea level [mbsl], Pc1: 937–980 m depth below seafloor [mbsf], and Pc2: 908–917 mbsf, Pc3: 757–780 mbsf; C0010: 2524 mbsl, Pc1: 610 mbsf, and Pc3: 405 mbsf; C0006: 3872 mbsl, Pc1: 456 mbsf, and Pc2: 426 mbsf). We focused herein on the deepest pore pressure (Pc1) at each borehole to see the crustal deformation close to the subduction plate boundary.

The pore pressure change mainly reflects the contributions from the following components: volumetric strain change driven by the crustal deformation in the accretionary prism several kilometers above the plate interface (Davis et al., 2006), ocean tides and other oceanographic loading (Araki et al., 2017), and dynamic deformation due to the passage of seismic waves radiated from earthquakes (Katakami et al., 2020). We removed the oceanic loading using the reference pressure sensor on the seafloor co-located for each observatory (Araki et al., 2017). The value of coefficient (α) for the reference pressure is obtained by the method of least squares for $R=(Pc1-\alpha*Pc0)$.

If the pore pressure change is derived from elastic deformation, we can linearly convert it to the volumetric strain change. From previous studies, the conversion factors are obtained for each Pc1 at C0002 (5.7 kPa/ μ strain), C0010 (4.7 kPa/ μ strain), and C0006 (6.0 kPa/ μ strain) (Davis et al., 2006; Wallace et al., 2016; Araki et al., 2017). Therefore, monitoring of the pore pressure change is useful to evaluate the crustal deformation.

Figure 3 shows the time history of Pc1 at each borehole from March to April in 2020 with the oceanic signals reduced, which suggests that pore pressure change at C0002 is similar to ramp function. This feature could not be explained from the oceanic loading. If this change is due to crustal deformation, the volumetric strain at C0002 had a significant dilation change (estimated as -0.14μ strain) on March 17–26, 2020. By contrast, no significant change was observed at C0006. As mentioned in the introduction section, C0010 has already the unrecognized fluctuation before the pore pressure event. This means that we have to extract the crustal deformation component if the pore pressure event is driven by SSE, which is to be discussed in the following sections.

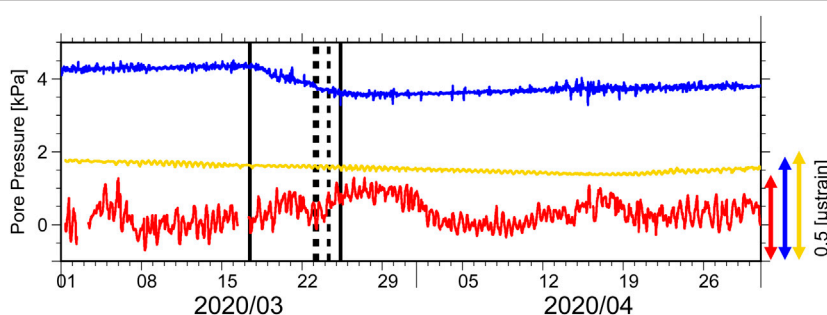


FIGURE 3 | Time history of the pore pressure at the deepest stations (Pc1) of each borehole observatory with a volumetric scale for each station (vertical double arrows). The oceanic signals are reduced by the reference hydraulic pressure gauge on the seafloor. The bold lines represent the onset/termination time of the pore pressure event. The dotted lines represent the origin times of the sVLFs (**Table 1**).

sVLFE Activities Beneath the Borehole Observatories

Figure 4A shows past sVLFE activities off Tonankai and Nankai regions, which indicates that sVLFE is active locally around the strong coupling regions of the megathrust earthquakes. In the target area, sVLFE had occurred in the marginal part of the 1944 Tokai earthquake and the transition zone to the 1946 Nankai earthquake. From the previous results, the previous SSE source

areas coincided with the sVLFE locations (Sugioka et al., 2012; Obara and Kato, 2016), and the sVLFEs were temporally excited during the SSE (Araki et al., 2017; Nakano et al., 2018).

We found the five sVLFEs between March 23 and 24, 2020 from the broadband velocity seismograms of the DONET stations along Nankai Trough. The sVLFE catalog during that period, indicating that one of them is a doublet event spatiotemporally, is shown in **Table 1**. We applied a centroid moment tensor waveform inversion to the broadband velocity seismometers at

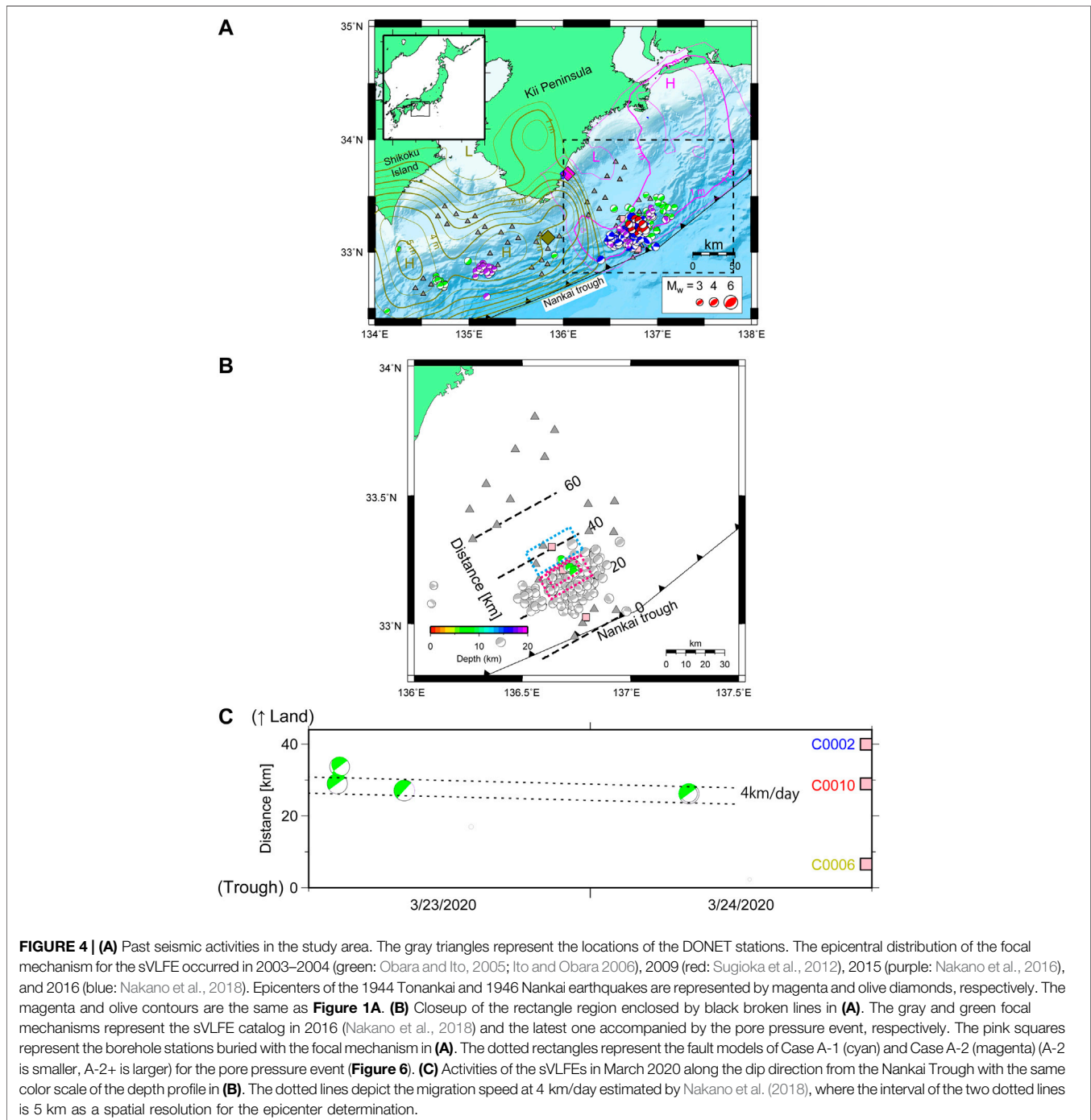


TABLE 1 | sVLFE catalog in March 2020.

Date	Time	Latitude	Longitude	Depth (km)	Mw
03/23/2020	02:24:39	33.22	136.72	7.0	3.4
	02:32:58	33.25	136.68	6.0	3.3
	08:10:30	33.21	136.74	6.0	3.5
03/24/2020 (Doublet)	08:19:58	33.20	136.74	7.0	2.8
	08:21:10	33.20	136.74	7.0	3.4

each DONET station (Nakano et al., 2018) during the pore pressure event to determine the source location, fault orientation parameters, and moment magnitude of the sVLFEs. The obtained source location and moment magnitudes are listed in **Table 1**, where horizontal and vertical resolution is 5 and 2 km, respectively.

Figure 4B shows the focal mechanisms of the sVLFEs were low-angle thrust-type faults largely along the plate interface. These results are consistent with previous sVLFE activities (**Figure 4A**). The hypocenter distribution of the sVLFEs in 2020 overlapped the source regions of past sVLFEs in part of the large slip area of the great 1944 Tonankai earthquake (Ichinose et al., 2003).

The time history of the sVLFEs along the horizontal distance from the trench is shown in **Figure 4C**. As suggested in **Figures 4B,C**, the spatiotemporal change of the five sVLFEs in 2020 appeared to be characterized by a migration from downdip to updip toward the trench (**Figure 4C**). This result is similar to the previous SSE in 2016, whose migration rate was approximately 4 km/day (Nakano et al., 2018).

These results imply that the pore pressure event is driven by SSE migrating toward the trench and the time history of pore pressure at C0010 may partly have crustal deformation component, which is discussed in the following sections.

ESTIMATION OF THE ONSET/TERMINATION TIME AND THE PORE PRESSURE CHANGE AT C0002

The duration time of the SSE was estimated in days (Araki et al., 2017; **Table 2**), whereas the origin time of the sVLFE was estimated in seconds (or less). This might cause difficulty to investigate the relationship between the SSE and sVLFE. One of the reasons of the daily solution for the SSE duration time is that the change in rate of the pore pressure at the beginning and ending of SSEs appears insufficiently clear, which is difficult to estimate the duration time precisely. We compensated for the gap of the time precision by trying to quantitatively estimate the amount of the pore pressure change and the onset/termination time of the pore pressure event in March 2020 by fitting regression lines, focusing on C0002 because of its simple behavior.

The time history of the pore pressure change at C0002 could be separated into three periods as before, during, and after the pore pressure event (**Figure 3**). Before and after the pore pressure event, linear regression analysis is well applicable with trend

negligible. During the pore pressure event, however, a temporal decrease of the pore pressure was observed (hidden in **Figure 3** because of decimation operation), which could not be explained by the regression analysis and will be discussed later.

To avoid a wrong regression estimation caused by such an unrecognized perturbation during the pore pressure event, we only estimated the two regression lines before and after the pore pressure event by treating the onset and the termination time of the pore pressure event as unknown parameters. The remaining regression line during the pore pressure event can be obtained by connecting both edges of the two regression lines before and after the pore pressure event, which gives the change amount of the pore pressure during the event. We select the input data span from March 1 to April 9, 2020 so that the periods of before, during and after the pore pressure event is comparable, where this choice of the date range is not critical for the following result. We

TABLE 2 | Updated summary of the borehole pressure signals and SSE characteristic.

Dates	Polarity	$\Delta\varepsilon_v$ C0002 (μ strain)	$\Delta\varepsilon_v$ C0010 (μ strain)	Slip (cm)	Location (km)	Slip region
*Mar 11–13, 2011	Dilation	−0.32	−0.46	2–4	<25	Updip
Feb 14–Apr 26, 2012	Contraction	0.05	0.07	1–2	>36	Downdip
Dec 5–14, 2012	Mixed	−0.08	0.15	1–2	25–36	Intermediate
Mar 6–19, 2014	Mixed	−0.07	0.13	1–2	25–36	Intermediate
Nov 19–Dec 1, 2014	Contraction	0.04	0.05	1–2	>36	Downdip
Oct 8–Nov 4, 2015	Mixed	−0.24	0.15	2–4	25–36	Intermediate
*Oct 8–Nov 4, 2015	Dilation	−0.24	−0.15	2–4	<25	Updip
*Apr 3–18, 2016	Dilation	−0.48	N/A	2–4	<25	Updip
Aug 10–24, 2016	Mixed	−0.05	0.14	1–2	25–36	Intermediate
Jul 4–16, 2017	Mixed	−0.11	0.11	1–2	25–36	Intermediate
Apr 26–May 7, 2018	Mixed	−0.07	0.30	2–4	25–36	Intermediate

$\Delta\varepsilon_v$: the compressional volumetric strain is positive, whereas the dilatational one is negative.

Location: distance from the center for the slip region of 20–40 km width to the trench landward, as shown by the equidistant lines in **Figure 4B**.

Shaded region: the result from Araki et al. (2017).

*SSE accompanied by sVLFEs.

adopted the least absolute value (L1 norm) to the evaluation function for all input data of 20 min sampling, moving the onset and the termination time during the data period at a 20 min interval. Although we also investigated other methods, such as the least squares method (L2 norm) with the time sampling changed, these methods could not obtain reasonable solutions.

Table 3 shows the results of best solution for each sensor at C0002. The standard deviations of the onset/termination time and the pore pressure change are 1.0 days and 1.0 hPa (1.1 days and 1.7 hPa for Pc3), respectively. Without the temporal decrease, the standard deviations are 9 h and 0.4 hPa, respectively. The time history of the pore pressure change compared with the regression lines of the analytical solution is shown in **Figure 5**. Since the time lag from the origin time of sVLFEs to the termination time of the pore pressure event (1 day and 20 min) is larger than the standard deviation (0.375 or 1.0 days), we statistically conclude that the sVLFE occurred during the pore pressure event.

From **Table 3** and **Figures 5A–C**, the best solution of Pc3 has shorter duration time due to the later onset and the earlier termination times than Pc1/Pc2. **Figure 5C** also shows that ocean noise component for Pc3 is significantly larger than that for Pc1 and Pc2. This means that the determination of the onset/termination time of the pore pressure event for Pc3 may not be robust. **Figure 5D** shows another regression combination for Pc3, assuming the onset/termination time is the same as Pc1 and Pc2, which seems also consistent with observation data. The amounts of pore pressure changes for Pc3 in **Figures 5C,D** are -10.3 and -10.0 hPa, respectively. This result suggests that the amplitude of ΔP for Pc3 is larger than Pc1 and Pc2, which is consistent with static dislocation model (Okada, 1992) due to the free surface condition.

POSSIBILITY OF SSE FOR THE PORE PRESSURE EVENT

In **Figure 3**, the unrecognized fluctuation of pore pressure at C0010 seems to be classified into (about daily) periodic and systematic components of non-crustal deformation. The amplitude of the systematic component is sometimes greater than that of periodic one. This means that it is not reasonable to estimate the onset/termination time and the amount of pore pressure change at C0010 solely from the time history. To evaluate the amount of pore pressure change statistically, we have to classify the time history of pore pressure change at C0010 into the signal (crustal deformation component), the systematic error and periodic perturbation.

TABLE 3 | Estimation results of pore pressure change due to the SSE in 2020.

Station	Onset	Time	Termination	Time	ΔP_{C0002} (hPa)
Pc1	17 March	11:20	25 March	08:40	-8.0
Pc2	17 March	11:20	25 March	08:40	-7.9
Pc3	18 March	14:00	25 March	04:40	-10.3 (-10.0)*

(*) is the value in case of both the onset/termination time is the same as Pc1 and Pc2 as shown in **Figure 5D**.

In this section, we try to find a reasonable time series of pore pressure change at C0010 and discuss the validity of identifying the pore pressure event as SSE by considering our results mentioned above and characteristics of previous SSEs.

Possible Cases of the Onset/Termination Times and Volumetric Strain Change at C0010

First, we compare the pore pressure event with previous SSEs which accompanied sVLFE. From **Table 2**, the corresponding SSEs occurred in 2011, 2015 and 2016. Unfortunately, the pore pressure record at C0010 was not obtained for SSE in 2016. Hence, we focus on the SSEs in 2011 and 2015. Since these SSEs occurred before the replacement of sensors at C0010, the quality of pore pressure record at C0010 was as good as C0002. For these SSEs, the onset and termination time of the pore pressure change is almost simultaneous between C0002 and C0010 (Araki et al., 2017). Therefore, we focus on the pore pressure records of the pore pressure event between the onset and termination times estimated in the preceding section (17 March 11:20 to 25 March 08:40; as listed in **Table 3**) as shown in **Figures 5A,B**.

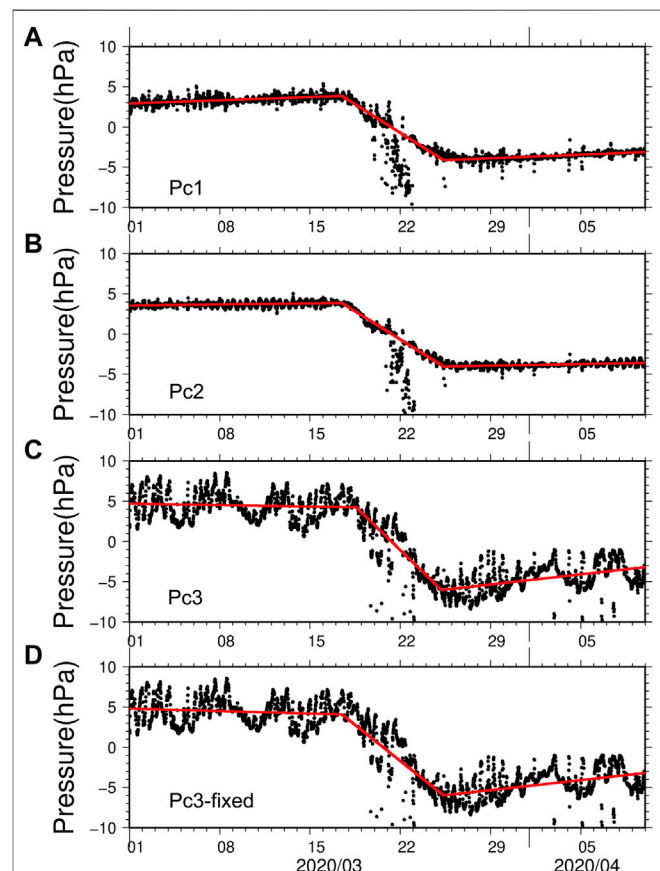


FIGURE 5 | Time history of the pore pressure (dotted black: 20 min sampling) with the fitting regression lines (red) for (A) Pc1, (B) Pc2, (C) Pc3, and (D) Pc3 under the same time of onset and termination as Pc1 and Pc2.

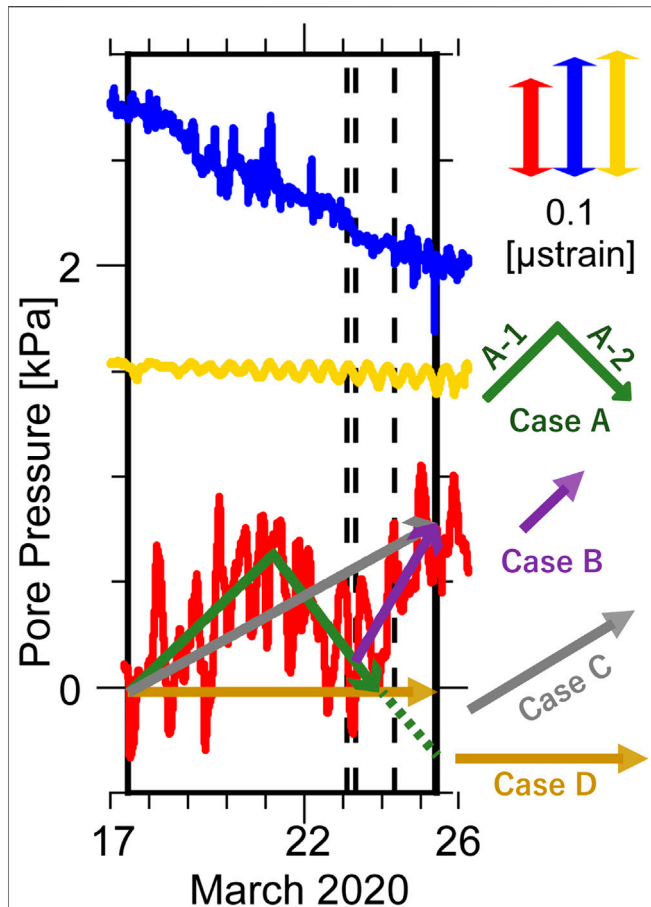


FIGURE 6 | Close up of the time history of the pore pressure (Figure 3) during the event, where the onset/termination time is determined by Figures 5A,B. Arrows indicate possible cases for the time histories of crustal deformation component at C0010 determined by regression lines (see text). The dotted lines represent additional Cases A-2+ and C+ as listed in Table 4.

On the basis of the time history of pore pressure at C0010 during the event, we assume four possible cases as shown by arrows in Figure 6. Case A is derived from the SSE in 2015, which is divided into the increase (A-1) and decrease (A-2) cases of the pore pressure. This means that the crustal deformation of SSE is composed of Cases A-1 and A-2, where the latter part of increase at C0010 in Figure 6 is treated as unrecognized noise component. In addition, we also assume Case A-2+, whose dilation lasts for the dilation of C0002 time as shown by dotted line in Figure 6, in according to SSE in 2015 (Araki et al., 2017). Case B assumes that the latter part of increase is the crustal deformation component. Case C assumes that the decrease of pore pressure is the unrecognized noise and the crustal deformation is described as monotonic increase. Case D assumes that there is no signal like C0006.

To estimate the pore pressure change at C0010 for each Case and onset times for Cases A-2 and Case B, we apply the same regression analysis as Figure 5 to C0002 by treating the error of periodic component of fluctuation approximately as a Gaussian distribution. Figure 6 shows the best solutions of regression lines

for each Case. The amounts of volumetric strain changes at C0002 and C0010 for each Case and the onset times for Case A-2 and Case B are listed in Table 4, where the volumetric strain changes at C0002 for Cases A-1, A-2 and B are determined by the onset/termination times under the constant decrease rate of the best regression analysis in Figure 5. The standard deviations of the pore pressure change at C0010 and onset time are 2.1 hPa (~0.045 μstrain) and 0.86 days, respectively.

Statistical Evaluation of Confidence for Each Case of Pore Pressure Change at C0010

As mentioned in Section Possible Cases of the Onset/Termination Times and Volumetric Strain Change at C0010, we assume that the pore pressure change at C0010 contains crustal deformation component between the onset and termination times estimated from C0002. However, there is still possibility that the pore pressure change at C0010 during that time span is due to unrecognized fluctuation. In this section, we try to evaluate the statistical confidence of the crustal deformation component at C0010 for each Case in Figure 6.

To verify the possibility of crustal deformation at C0010 due to SSE statistically, we adopt the minimum square method for the regression lines of all Cases in Figure 6,

$$S(i) = \{y(t_i) - f_{(A,B,C,D)}(t_i)\}^2, \tag{1}$$

$$U = \{S(1), S(2), \dots, S_n\}, \tag{2}$$

where t and i are time and its index, respectively. y and $f_{(A,B,C,D)}$ are observational data and the regression analysis in Figure 6, respectively. n is the number of 20 min sampling for each Case as listed in Table 4. For the pore pressure event (Figure 6), the average and standard deviation of $S(i)$ in $U_{(A,B,C,D)}$ are obtained as \bar{S} and σ .

Since the last SSE occurred in May 2018 (Table 2), we can treat the yearlong data from 16 March in 2019 to 16 March in 2020 (Figure 7) as the reference of the unrecognized fluctuation. If the time series of pore pressure change at C0010 in Figure 6 were due to the unrecognized fluctuation, similar change would occur in

TABLE 4 | Possible cases of the volumetric strain change due to the SSE in 2020.

	Polarity	C0002 (μstrain)	C0010 (μstrain)	Onset Time (March 2020)	Termination Time (March 2020)	Sample (n)
A-1	Mixed	-0.066	+0.14	17 11:20	21 04:00	
Case	↓	↓	↓			
A-2	Dilation	-0.074	-0.14	21 04:00	23 20:40	461*
A-2+			-0.22	21 04:00	25 08:40	569*
Case	Mixed	-0.066	+0.14	23 06:20	25 08:40	152
B						
Case	Mixed	-0.14	+0.17	23 06:20	25 08:40	569
C						
Case	—	-0.14	0.0	23 06:20	25 08:40	569
D						

*Total sample of Case A-1 and A-2 (+).

Compressional volumetric strain is positive, whereas the dilatational one is negative.

the yearlong period. For the yearlong data, we calculate \bar{S} and σ' with the same number of sampling as the regression lines for each Case (Table 4), moving the time window by one sampling at a time from the beginning to the end of the yearlong data.

If the pore pressure change at C0010 in Figure 6 is significantly different from the unrecognized fluctuation (Figure 7), there should be always significant difference between \bar{S} and \bar{S}' for all the time window in the yearlong period. Here, we apply two-sample t-test between (\bar{S}, σ) and (\bar{S}', σ') for each moving time window to verify whether $\bar{S} < \bar{S}'$ or not, where the value of t statistics is described as

$$t = \frac{\bar{S}' - \bar{S}}{\sqrt{(\sigma^2 + (\sigma')^2)/n}} \quad (3)$$

and t distribution is approximated as the standard normal distribution function because of high degree of freedom ($n-1 > 100$).

Figure 8 shows the time history of t statistics for each Case. Figures 8A,B show that the value of t statistics is basically positive (>5). For Case (A-1) to (A-2+), the (negative) minimum value of the t statistics is -0.84 for the time window between 27 April 08:40 and 5 May 05:40 in 2019 and -0.74 between 31 March 20:00 and 8 April 16:40 (dotted lines in Figure 7). These mean that the probability of $\bar{S} < \bar{S}'$ is 20% and 27%, respectively. For the other Cases, Figure 8 shows that there are many time windows with the t statistics less than -5, where the probability of $\bar{S} < \bar{S}'$ is less than 0.01%. From these results, Cases B, C, and D could not be distinguished from the unrecognized fluctuation, and the reliability of Case (A-1) to (A-2+) for crustal deformation component is at most 20% because of low S/N ratio. In the following sections, we try to enhance the reliability of pore pressure change at C0010 by considering sVLFE activities as well as pore pressure changes at other borehole sites.

Relationship Between the Volumetric Strain Change and Fault Location of SSE

Because of the insufficient number of borehole observatories, it is practically difficult to estimate the fault parameters by inversion method. In this study, we assume that SSE occurred on the plate

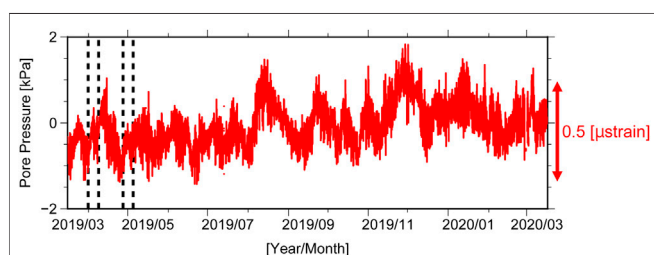


FIGURE 7 | Time history of the pore pressure at the deepest stations (Pc1) of C0010 with a volumetric scale for each station (vertical double arrows) from one year before to the one day before the onset time of the pore pressure event. Two pairs of vertical dotted lines indicate the time windows of best fitting regression lines for Case (A-1) to (A-2+) as indicated by vertical arrows in Figure 8.

interface beneath the borehole observatories, according to the previous method (Wallace et al., 2016; Araki et al., 2017).

We set up the fault location, fault width, and fault displacement as unknown parameters which well explain the two volumetric strain changes at C0002 and C0010. Considering the spatial resolution due to limited observations, we assume that the epicentral location for the center point of fault is along the line between C0002 and C0010, the width is 20 or 40 km, and the displacement is 1-2 or 2-4 cm. The forward modeling assumed a simple rectangular fault model (Okada, 1992) in a homogeneous elastic medium with a Poisson's ratio of 0.35 and a rigidity of 20 GPa, which is the same condition as Araki et al. (2017). The simplified fault model assumed that the direction angles of strike, dip, and rake were 239° (along subduction direction), 6°, and 90°, respectively, where the strike direction was orthogonal to the equidistant lines from the trench in Figure 4B.

For the previous SSEs, the polarities of the volumetric strain changes at C0002 and C0010 reflects the relative location between the two sites and SSE (Araki et al., 2017). Following the result, we classified the polarities into three patterns: 1) Mixed pattern with a dilation at hole C0002 and a contraction at C0010 under the condition of a similar magnitude between them, 2) Dilation at both sites, and 3) Contraction at both sites. These patterns can roughly constrain the fault location relative to the two sites. We categorized the possible slip regions into three on the basis of the distance from the trench to the center for the 20-40 km-wide fault (Table 2): updip region (<25 km) for the Dilation polarity, intermediate region for the Mixed (25-36 km), and downdip region (>36 km) for the Contraction.

Constraint of sVLFE Migration on the SSE Fault Models

Next, we apply the fault estimation to the volumetric strain change for each Case, where the polarity is summarized in Table 4. Case A has combination of the Dilation (A-1) and the Mixed (A-2) polarities. This means the fault slip migrated from the intermediate region (A-1) to updip (A-2). Case B and Case C have the Mixed polarity with the fault slip in the intermediate region. Case D has the Dilation polarity with the fault slip in the updip region.

From recent results, the sVLFEs were detected from the DONET seismic records during the SSEs in 2011 (To et al., 2015), 2015 (Nakano et al., 2016), and April 2016 (Nakano et al., 2018) [(*)], Table 2), whereas the sVLFE has not been detected during the other SSEs. Nakano et al. (2018) suggested that whether the SSE will be accompanied by an sVLFE or not is dependent on the source location. If the SSE is in the downdip or intermediate region, sVLFE does not occur. If the SSE migrates to the updip region and reach the source regions of sVLFEs, sVLFEs occur during the SSE.

As investigated in the Section *sVLFE Activities Beneath the Borehole Observatories*, five sVLFEs were detected during the pore pressure event, migrating toward the updip region. Their focal mechanisms of the sVLFEs were on the subduction plate

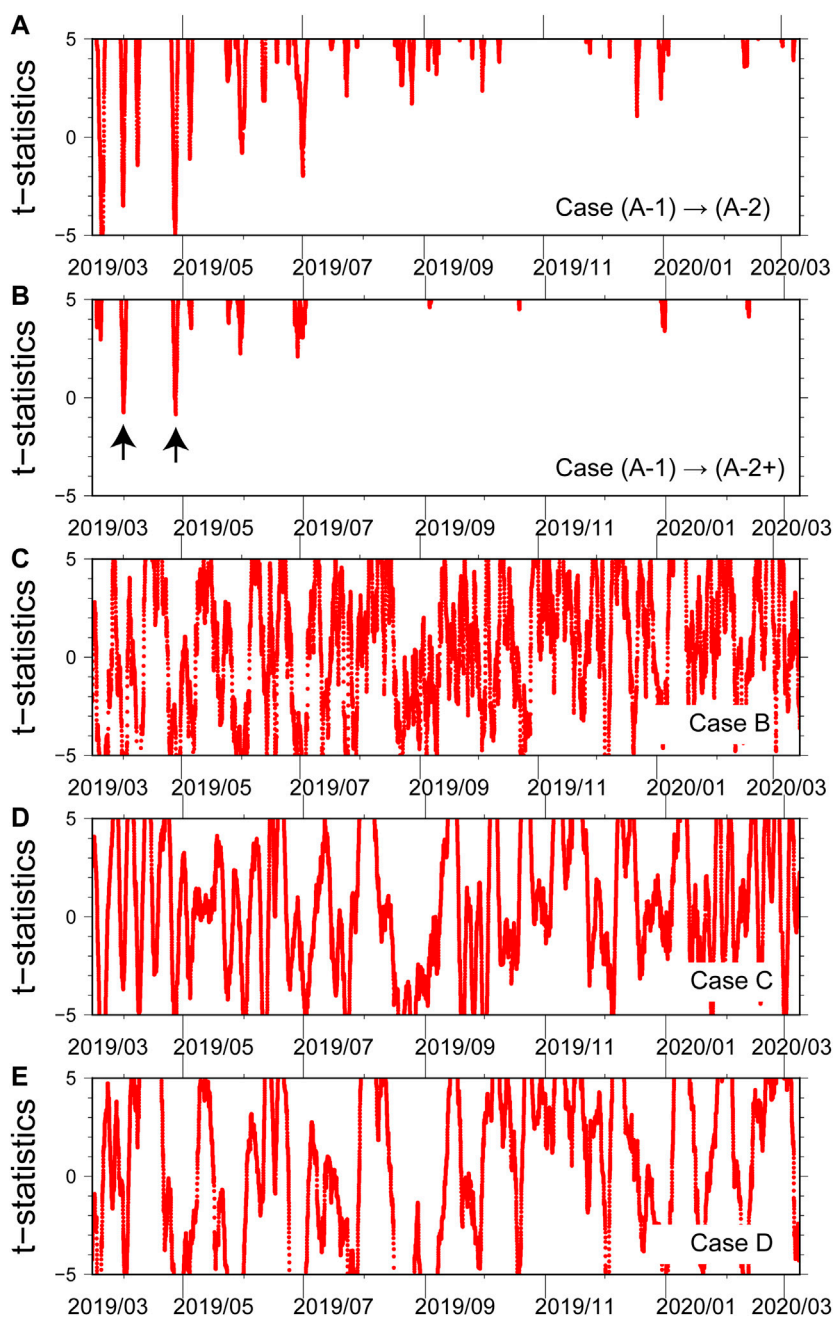


FIGURE 8 | Time history of t -statistics in Eq. (3) for each Case. Horizontal axis is origin time of fitting time window. Positive value of t -statistics means regression lines explain crustal deformation component due to SSE better than unrecognized fluctuation. Vertical arrows indicate the minimum value of t -statistics for Case (A-1) to (A-2+), where corresponding time windows are indicated by two pairs of vertical dotted lines in Figure 7.

boundary with low dip angles (Figure 4C), which meets the dip angle subducting there. These features are consistent with the suggestion by Nakano et al. (2018) for the previous SSEs as mentioned above.

Considering these results, Case C is not acceptable because the pore pressure event was accompanied by sVLFs which needs slip in the updip region. In addition, since the epicentral location are of sVLFs are close to C0010 as shown in Figure 4, Case D is not

acceptable because no signal at C0010 contradicts the sVLF activity during the pore pressure event (Figure 4B).

Estimation of the Reasonable SSE Fault Model Without Depth Fixed Condition

To investigate the validity of Cases A-C, we try to find the best fit model for each Case by adopting alternative grid search without

depth fixed on the subduction plate boundary, confirming whether the fault location is on the subduction plate boundary or not and whether its slip migration is toward the updip region or not.

In our model, the aspect ratio of the fault was assumed to be 2.0, and the directions of the strike, dip, and rake were fixed as 240°, 6°, and 90°, respectively. The other parameters were the same as those of the simplified model in the Section *Statistical Evaluation of Confidence for Each Case of Pore Pressure Change at C0010*. We adopted grid search by fitting the location, size, and depth of the fault compared with the two volumetric strain changes between each Cases A-C (Table 4) and the calculation. The grid intervals of the location for the fault center point, size, and depth were 0.01 time of distance between C0002 and C0010, 2 km, and 1 km, respectively. The uniform slip was assumed as purely dip of reverse type. Its amount was estimated from the least minimum square.

Fault parameters of the best fit model for Cases A-C are listed in Table 5. All the best fit model for each Case can quantitatively explain the observed volumetric strain changes at the two sensors (C0002 and C0010), where we do not use the information about no signal at C0006 of Pc1 as input data for the fitting. Next, we compare the best fit models for each Case with the observational results analyzed in previous sections.

The fault location for the best fit model of Case A is shown in Figures 9, 4B, which suggests that Case A can also explain the slip migration toward the updip region under the free constraining condition for the focal depth. Since Figure 4B shows that the epicenters of sVLFE are in the fault model of Case A-2, Case A is also consistent with the timing of the sVLFE activity.

In previous SSEs accompanied sVLFE in 2011 and 2015, the rate of pore pressure change at C0010 kept constant until the termination time (Araki et al., 2017). Therefore, we also assume that condition (Case A-2+) as shown by dotted line extended from Case A-2 in Figure 6, where the amount of volumetric strain change at C0010 is $-0.22 \mu\text{strain}$ as listed in Table 4. The best fit model of Case A-2+ is shown in Figure 9C; Table 5, whose fault geometry is almost the same result as Case A-2.

Case B suggests that the volumetric strain is changed from the Dilation polarity to the Mixed on the way of Case A-2. Since the amount of the volumetric strain change for Case B is almost the same as Case A-1 (Table 4) due to similar rate and period (Figure 6), the best fit model of Case B is also the same as Case A-1. These results suggest that the fault slip migrates from the updip on the way of Case A-2 to intermediate region in Case B, which could not explain the sVLFE activity with the migration toward the updip region (Figure 4) during Case B. Therefore, we conclude that Case B is not acceptable.

The best fit model of Case C is shown in Supplementary Figure S1; Table 5, which has relatively large magnitude with larger slip and wider area covering epicentral locations of C0002 and C0010. This model is expected to have significant volumetric strain change at C0006 ($0.042 \mu\text{strain}$ in Table 5). However, Figures 3, 6 suggest that the observed one seems no significant signal at C0006 during the event. Therefore, we conclude that Case C is not acceptable.

From these results and *t*-test in Section *Statistical Evaluation of Confidence for Each Case of Pore Pressure Change at C0010*, assuming that crustal deformation component of the observed volumetric strain change due to SSE is treated as Case A, we can explain the migration of sVLFE toward the updip region during the SSE reasonably (hereafter, we refer to this event as the SSE in 2020). Since Case A is similar to the time history of pore pressure change for the SSE in 2015, we discuss the characteristics of the SSE in 2020 by comparing with it in the following section.

SUMMARIES AND DISCUSSIONS

First, we discuss the difference of the magnitude between the SSEs in 2020 and 2015. The amplitude of the pore pressure changes for Case A (Table 4) for both C0002 and C0010 sites were smaller than that of the SSE in 2015 (Table 2). The duration of the SSE in 2020 (10 days) was shorter than the SSE in 2015, which was 28 days. As shown in Table 1, five sVLFEs (M_w 2.8 to 3.4) during the SSE in 2020 were detected in 30 h. The total number of sVLFEs ($M_w \geq 3.4$) during the SSE in 2015 was more than 20 over 20 days (Takemura et al., 2019), indicating that the cumulative moment magnitude of the sVLFE in 2020 should be smaller than that in 2015. These results suggest that the slip process of the SSE in 2020 is similar to the SSE in 2015 but with a smaller magnitude.

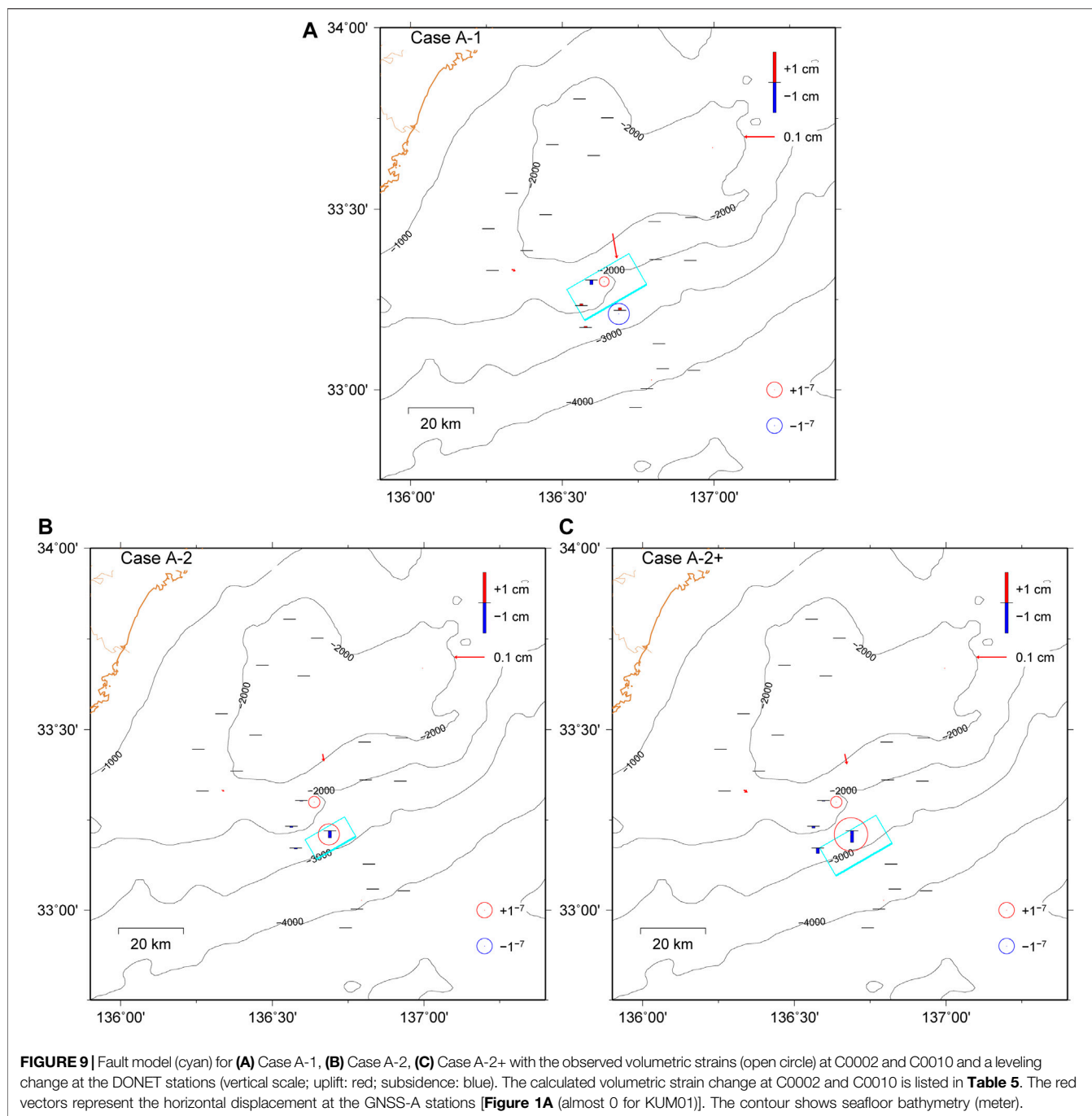
Figure 10 shows the catalog of the pore pressure and the volumetric strain transient at the C0002 and C0010 boreholes with the simplified fault models for the previous SSEs in Table 2 and Case (A-1) to (A-2) in Table 4 applied to the SSE in 2020 occurring between the origin and termination times as listed in Table 3. As depicted in Figure 10; Table 2, all the duration times for the SSEs, except in 2012, were much shorter than the time resolution of the SSE detection from GNSS-A (0.2 years; Yokota and Ishikawa, 2020). We also estimated the onset and the termination time of the SSE in 2020 in 20 min. Owing to the high time resolution, we estimate the slip process of the SSE in 2020 as migration from the intermediate to the updip regions crossing over beneath C0010.

TABLE 5 | The best fit fault model for Cases A-C.

Case	Latitude	Longitude	Depth (km)	Width (km)	Slip (cm)	Mw	C0002* (μstrain)	C0010* (μstrain)	C0006 (μstrain)
A-1(B)	33.28	136.65	5	22	0.83	5.0	-0.066	+0.14	+0.001
A-2	33.20	136.69	5	14	2.0	5.0	-0.074	-0.14	+0.001
A-2+	33.18	136.70	5	20	1.7	5.2	-0.074	-0.22	+0.0002
C	33.23	136.68	7	36	4.1	5.7	-0.14	+0.17	-0.042

*Input data for the least minimum square method in grid search.

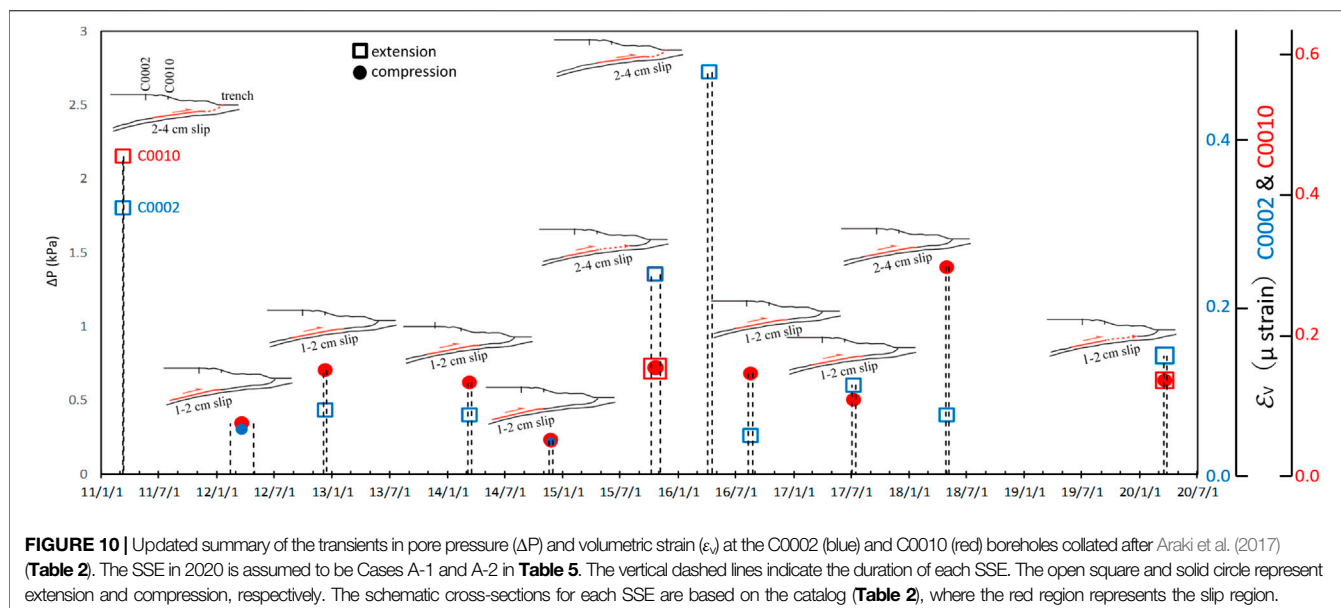
Compressional volumetric strain is positive, whereas the dilatational one is negative.



Because of no significant signal at C0006, we conclude that the slip of the SSE in 2020 did not reach very shallow part of plate interface beneath C0006 as shown in **Figure 4B**. **Figure 4B** also shows that sVLF is not active around the epicentral location of C0006, where the slip amount of the 1944 Tonankai earthquake is relatively small. These results indicate that the volumetric strain just below C0006 might not be accumulated because of stable frictional property near the trench (e.g., Scholtz, 1998), or there is strong coupling enough to refrain from sVLF activity. This question is to be solved by long-term monitoring at C0006. The results demonstrate that

monitoring the pore pressure change is a powerful tool for precisely estimating the region and duration of SSEs. If we estimate the fault model promptly during the pore pressure changes on the basis of our analysis, we can judge the possibility of sVLF activity in advance of the occurrence.

We could not identify a significant increase in the moment release rate and shorter recurrence interval of the SSE from **Figure 10**. However, unrecognized SSEs (Katakami et al., 2020) could have possibly been buried in a large noise component. In addition, as mentioned in the Section *Estimation of the Onset/Termination Time and the Pore Pressure Change at C0002*, there



is the temporal decrease of pore pressure during the SSE in 2020 in Figure 5. Because it lasted for several days, which could be explained from the temporal change of slip velocity during the SSE in 2020 rather than the excitation of the local sVLFE or tremors (Barbour 2015) because of the significantly longer period without a comparable increase. Therefore, the development of a noise reduction analysis using other borehole sensors and/or a combination of the nearby hydraulic pressure gauges of DONET would be important in identifying missed SSEs.

The leveling change in all DONET stations is also shown in Figure 9, implying that the expected leveling change was not sufficient for detection (i.e., 0.3 hPa at most). The observed noise level of the DONET pressure gauge was approximately 1–2 hPa (1–2 cm for leveling change) (Suzuki et al., 2016; Takemura et al., 2019). This small leveling change was partly due to low dip angle around the Nankai Trough (e.g., Sugioka et al., 2012).

We discussed the detectability of the horizontal displacement by showing the horizontal displacement of Case A on the seafloor at the GNSS-A stations (Figure 1A) (red arrows, Figure 9). The displacement is expected to be small (0.2 cm at most) if the fault slip is uniform. If the actual fault slip distribution changes spatiotemporally (Fukuda, 2018); thus, the SSE in 2020 can still be detected from other observations, such as GNSS-A (Yokota and Ishikawa, 2020). This will be the focus of our future work.

DATA AVAILABILITY STATEMENT

DONET observation data and the catalog of sVLFE estimated by Nakano et al. (2016) and Takemura et al. (2019) are available via the website of the National Research Institute for Earth Science and Disaster Resilience (2019) and the Slow Earthquake Database website (Kano et al., (2018); <http://www-solid.eps.s.u-tokyo.ac.jp/~sloweq/>), respectively. Borehole data is available from the website of the J-SEIS (JAMSTEC Ocean-bottom Seismology Database; <https://join-web.jamstec.go.jp/join-portal/>).

AUTHOR CONTRIBUTIONS

KA estimated the pore pressure change, onset, and termination time of the SSE in 2020. TI estimated the fault model of the Updip region for the SSE in 2020. MN estimated the focal mechanisms of the sVLFEs. TK also checked the pore pressure change independently as double check. EA led the DONET system installation. EA, TK, and YM installed the borehole observatories. TH, NT, and SK commented on improving the manuscript. TK, KS, and KS installed the real-time monitoring system of borehole observatory and DONET, making some figures automatically. SY and TN compiled the SSE catalog.

FUNDING

This work was partly supported by the Japan Society for the Promotion of Sciences (JSPS), Grant-in-Aid for Scientific Research (KAKENHI) Grant Number JP16H06477, JP17K19093, JP19H02411, and JP20H02236.

ACKNOWLEDGMENTS

Generic Mapping Tools (Wessel et al., 2013) was used to create figures. The authors would like to thank reviewers for their helpful comment to improve our manuscript, and Editor Keiichi Tadokoro for his expeditious handling.

SUPPLEMENTARY MATERIAL

The Supplementary Material for this article can be found online at: <https://www.frontiersin.org/articles/10.3389/feart.2020.600793/full#supplementary-material>.

REFERENCES

- Araki, E., Saffer, D. M., Kopf, A. J., Wallace, L. M., Kimura, T., Machida, Y., et al. (2017). Recurring and triggered slow-slip events near the trench at the Nankai Trough subduction megathrust. *Science* 356, 1157–1160. doi:10.1126/science.aan3120
- Ariyoshi, K., Matsuzawa, T., Ampuero, J.-P., Nakata, R., Hori, T., Kaneda, Y., et al. (2012). Migration process of very low-frequency events based on a chain-reaction model and its application to the detection of preseismic slip for megathrust earthquakes. *Earth Planets Space* 64, 693–702. doi:10.5047/eps.2010.09.003
- Ariyoshi, K., Nakata, R., Matsuzawa, T., Hino, R., Hori, T., Hasegawa, A., et al. (2014a). The detectability of shallow slow earthquakes by the Dense Oceanfloor Network system for Earthquakes and Tsunamis (DONET) in Tonankai district, Japan. *Mar. Geophys. Res.* 35, 295–310. doi:10.1007/s11001-013-9192-6
- Ariyoshi, K., Matsuzawa, T., Hino, R., Hasegawa, A., Hori, T., Nakata, R., et al. (2014b). A trial derivation of seismic plate coupling by focusing on the activity of shallow slow earthquakes. *Earth Planets Space* 66, 55. doi:10.1186/1880-5981-66-55
- Barbour, A. J. (2015). Pore pressure sensitivities to dynamic strains: observations in active tectonic regions. *J. Geophys. Res. Solid Earth* 120, 5863–5883. doi:10.1002/2015JB012201
- Davis, E. E., Becker, K., Wang, K., Obara, K., Ito, Y., and Kinoshita, M. (2006). A discrete episode of seismic and aseismic deformation of the Nankai Trough subduction zone accretionary prism and incoming Philippine Sea plate. *Earth Planet Sci. Lett.* 242, 73–84. doi:10.1016/j.epsl.2005.11.054
- Dragert, G., Wang, K., and James, T. S. (2001). A silent slip event on the deeper Cascadia subduction interface. *Science* 292, 1525–1528. doi:10.1126/science.1060152
- Earthquake Research Committee of the Headquarters for Earthquake Research Promotion (2013). Long-term evaluation of nankai trough earthquake activity. 2nd Edition. Available at: http://www.jishin.go.jp/main/chousa/13may_nankai/nankai2_shubun.pdf (Accessed October 28, 2020).
- Fukuda, J. (2018). Variability of the space-time evolution of slow slip events off the Boso Peninsula, central Japan, from 1996 to 2014. *J. Geophys. Res. Solid Earth* 123, 732–760. doi:10.1002/2017JB014709
- Ichinose, G. A., Thio, H. K., Somerville, P. G., Sato, T., and Ishii, T. (2003). Rupture process of the 1944 Tonankai earthquake (Ms 8.1) from the inversion of teleseismic and regional seismograms. *J. Geophys. Res.* 108, 2497. doi:10.1029/2003JB002393
- Ide, S., Beroza, G. C., Shelly, D. R., and Uchida, T. (2007). A scaling law for slow earthquakes. *Nature* 447, 76–79. doi:10.1038/nature05780
- Ishikawa, T., Yokota, Y., Watanabe, S., and Nakamura, Y. (2020). History of on-board equipment improvement for GNSS-A observation with focus on observation frequency. *Front. Earth Sci.* 8, 150. doi:10.3389/feart.2020.00150
- Ito, Y., and Obara, K. (2006). Dynamic deformation of the accretionary prism excites very low frequency earthquakes. *Geophys. Res. Lett.* 33, L02311. doi:10.1029/2005GL025270
- Ito, Y., Obara, K., Shiomi, K., Sekine, S., and Hirose, H. (2007). Slow earthquakes coincident with episodic tremors and slow slip events. *Science* 315, 503–506. doi:10.1126/science.1134454
- Kaneda, Y., Kawaguchi, K., Araki, E., Matsumoto, H., Nakamura, T., Kamiya, S., et al. (2015). “Development and application of an advanced ocean floor network system for megathrust earthquakes and tsunamis?” in *Seafloor observatories*, (Chichester, United Kingdom: Springer Praxis Books), 643–663. doi:10.1007/978-3-642-11374-1_25
- Kano, M., Aso, N., Matsuzawa, T., Ide, S., Annoura, S., Arai, R., et al. (2018). Development of a slow earthquake Database. *Seismol Res. Lett.* 89, 1566–1575. doi:10.1785/0220180021
- Katakami, S., Kaneko, Y., Ito, Y., and Araki, E. (2020). Stress sensitivity of instantaneous dynamic triggering of shallow slow slip events. *J. Geophys. Res. Solid Earth* 125, e2019JB019178. doi:10.1029/2019JB019178
- Kawaguchi, K., Kaneko, S., Nishida, T., and Komine, T. (2015). “Construction of the DONET real-time seafloor observatory for earthquakes and tsunami monitoring,” in *Seafloor observatories*, (Chichester, United Kingdom: Springer Praxis Books), 211–228. doi:10.1007/978-3-642-11374-1_10
- Kitada, K., Araki, E., Kimura, T., Kinoshita, M., Kopf, A., and Saffer, D. (2013). “Long-term monitoring at C0002 seafloor borehole in Nankai Trough seismogenic zone,” in 2013 IEEE international underwater technology symposium (UT), Tokyo, March 5–8, 2013 (IEEE), 1–3. doi:10.1109/UT.2013.6519882
- Maeda, T., Obara, K., Shinohara, M., Kanazawa, T., and Uehira, K. (2015). Successive estimation of a tsunami wavefield without earthquake source data: a data assimilation approach toward real-time tsunami forecasting. *Geophys. Res. Lett.* 42, 7923–7932. doi:10.1002/2015GL065588
- Matsuzawa, T., Hirose, H., Shibasaki, B., and Obara, K. (2010). Modeling short- and long-term slow slip events in the seismic cycles of large subduction earthquakes. *J. Geophys. Res.* 115, B12301. doi:10.1029/2010JB007566
- Murotani, S., Shimazaki, K., and Koketsu, K. (2015). Rupture process of the 1946 Nankai earthquake estimated using seismic waveforms and geodetic data. *J. Geophys. Res.* 120, 5677–5692. doi:10.1002/2014JB011676
- Nakamura, T., Takenaka, H., Okamoto, T., Ohori, M., and Tsuboi, S. (2015). Long-period ocean-bottom motions in the source areas of large subduction earthquakes. *Sci. Rep.* 5, 16648. doi:10.1038/srep16648
- Nakano, M., Hori, T., Araki, E., Kodaira, S., and Ide, S. (2018). Shallow very-low-frequency earthquakes accompany slow slip events in the Nankai subduction zone. *Nat. Commun.* 9, 984. doi:10.1038/s41467-018-03431-5
- Nakano, M., Hori, T., Araki, E., Takahashi, N., and Kodaira, S. (2016). Ocean floor networks capture low-frequency earthquake event. *Eos*. doi:10.1029/2016EO052877
- National Research Institute for Earth Science and Disaster Resilience (2019). *NIED DONET*. Tokyo: National Research Institute for Earth Science and Disaster Resilience. doi:10.17598/NIED.0008
- Nishikawa, T., Matsuzawa, T., Ohta, K., Uchida, N., Nishimura, T., and Ide, S. (2019). The slow earthquake spectrum in the Japan Trench illuminated by the S-net seafloor observatories. *Science* 365, 808–813. doi:10.1126/science.aax5618
- Obara, K., and Ito, Y. (2005). Very low frequency earthquakes excited by the 2004 off the Kii peninsula earthquakes: A dynamic deformation process in the large accretionary prism. *Earth Planets Space* 57, 321–326. doi:10.1186/BF03352570
- Obara, K., and Kato, A. (2016). Connecting slow earthquakes to huge earthquakes. *Science* 353, 253–257. doi:10.1126/science.aaf1512
- Obara, K. (2002). Nonvolcanic deep tremor associated with subduction in southwest Japan. *Science* 296, 1679–1681. doi:10.1126/science.1070378
- Okada, Y. (1992). Internal deformation due to shear and tensile faults in a half-space. *Bull. Seismol. Soc. Am.* 82, 1018–1040.
- Saffer, D., Kopf, A., and Toczko, S. (2017). “The expedition 365 scientists,” in Proceedings of the international ocean discovery program, 365, November 23, 2017. Available at: publications.iodp.org (Accessed November 23, 2017). doi:10.14379/iodp.proc.365.103.2017
- Scholtz, C. H. (1998). Earthquakes and friction laws. *Nature* 391, 37–42. doi:10.1038/34097
- Schwartz, S. Y., and Rokosky, J. M. (2007). Slow slip events and seismic tremor at circum-pacific subduction zones. *Rev. Geophys.* 45, RG3004. doi:10.1029/2006RG000208
- Sugioka, H., Okamoto, T., Nakamura, T., Ishihara, Y., Ito, A., Obana, K., et al. (2012). Tsunamigenic potential of the shallow subduction plate boundary inferred from slow seismic slip. *Nat. Geosci.* 5, 414–418. doi:10.1038/ngeo1466
- Suzuki, K., Nakano, M., Takahashi, N., Hori, T., Kamiya, S., Araki, E., et al. (2016). Synchronous changes in the seismicity rate and ocean-bottom hydrostatic pressures along the Nankai Trough: a possible slow slip event detected by the Dense Oceanfloor Network system for Earthquakes and Tsunamis (DONET). *Tectonophysics* 680, 90–98. doi:10.1016/j.tecto.2016.05.012
- Takemura, S., Noda, A., Kubota, T., Asano, Y., Matsuzawa, T., and Shiomi, K. (2019). Migrations and clusters of shallow very low frequency earthquakes in the regions surrounding shear stress accumulation peaks along the Nankai Trough. *Geophys. Res. Lett.* 46, 11830–11840. doi:10.1029/2019GL084666

- To, A., Obana, K., Sugioka, H., Araki, E., Takahashi, N., and Fukao, Y. (2015). Small size very low frequency earthquakes in the Nankai accretionary prism, following the 2011 Tohoku-Oki earthquake. *Phys. Earth Planet. In.* 245, 40–51. doi:10.1016/j.pepi.2015.04.007
- Wallace, L. M., Araki, E., Saffer, D., Wang, X., Roesner, A., Kopf, A., et al. (2016). Near-field observations of an offshore Mw 6.0 earthquake from an integrated seafloor and subseafloor monitoring network at the Nankai Trough, southwest Japan. *J. Geophys. Res. Solid Earth* 121, 8338–8351. doi:10.1002/2016JB013417
- Wessel, P., Smith, W. H. F., Scharroo, R., Luis, J., and Wobbe, F. (2013). Generic mapping tools: improved version released. *Eos Trans. AGU* 94 (45), 409. doi:10.1002/2013EO450001
- Wiseman, K., and Bürgmann, R. (2011). Stress and seismicity changes on the sunda megathrust preceding the 2007 M_w 8.4 earthquake. *Bull. Seismol. Soc. Am.* 101 (1), 313–326. doi:10.1785/0120100063
- Yokota, Y., and Ishikawa, T. (2020). Shallow slow slip events along the Nankai Trough detected by GNSS-A. *Sci. Adv.* 6, eaay5786. doi:10.1126/sciadv.aay5786

Conflict of Interest: The authors declare that the research was conducted in the absence of any commercial or financial relationships that could be construed as a potential conflict of interest.

Copyright © 2021 Ariyoshi, Inuma, Nakano, Kimura, Araki, Machida, Sueki, Yada, Nishiyama, Suzuki, Hori, Takahashi and Kodaira. This is an open-access article distributed under the terms of the Creative Commons Attribution License (CC BY). The use, distribution or reproduction in other forums is permitted, provided the original author(s) and the copyright owner(s) are credited and that the original publication in this journal is cited, in accordance with accepted academic practice. No use, distribution or reproduction is permitted which does not comply with these terms.